CrossMark
click for updates

MOF-derived RuO$_2$/Co$_3$O$_4$ heterojunctions as highly efficient bifunctional electrocatalysts for HER and OER in alkaline solutions†

Haizhen Liu,[a] Guoliang Xia,[a] Ruirui Zhang,[a] Peng Jiang,[a] Jitang Chen[a] and Qianwang Chen*[ab]

The oxygen evolution reaction (OER) and hydrogen evolution reaction (HER) are key half reactions involved in electrochemical water splitting. The design of active and robust Co$_3$O$_4$-based electrocatalysts for overall water splitting in basic media is highly desirable but still remains a great challenge. Herein, a catalyst of a combined metal oxide heterojunction (RuO$_2$/Co$_3$O$_4$) was synthesized by directly annealing a MOF-derived Co−Ru complex under an air atmosphere. The catalyst shows a low OER and HER overpotential of only 305 mV and 89 mV at 10 mA cm^{-2} in 1 M KOH solution, respectively. It contains only a small amount of precious metal oxides, however, and demonstrates a better performance than most of the other Co$_3$O$_4$-based electrocatalysts reported at the present stage.

Introduction

Nowadays, more and more attention has been paid to the increase in global energy consumption and environmental problems due to burning fossil fuels associated with transportation and industry.[1,2] It is well known that splitting water into hydrogen and oxygen to store light or electric energy in the form of chemical bonds plays an important role in developing clean-energy technologies.[3-6] The water splitting reaction can be divided into two half-reactions: the hydrogen evolution reaction (HER) and the oxygen evolution reaction (OER), both of which are essential for the overall efficiency of water splitting. It has been demonstrated that electrochemical water splitting can be completed both in acidic and alkaline media. Unfortunately, the acid electrolyzers are hindered by the lack of efficient and low-cost counter electrode catalysts in acidic electrolytes. Therefore, tremendous efforts have been made to develop bifunctional catalysts in basic media due to the available alkaline oxygen evolution electrocatalysts.[7-10]

Precious-metal electrocatalysts, such as IrO$_2$ and RuO$_2$, are regarded as pioneering OER and HER catalysts, respectively, and can be implicated in a large window of solution pHs with high efficiencies.[11,12] But their low abundance and high cost

prevent them from large range of applications.[13,14] Alternatively, the first-row transition metal oxides are currently intensively investigated to improve the intrinsic activity as potential earth-abundant material candidates for water splitting electrocatalysts.[15-19] It has been reported that compounds of Co$_3$O$_4$-based compounds exhibit high activities toward OER,[20,21] which can serve as a low-cost replacement for the state-of-the-art RuO$_2$, due to its practical availability, environmentally benign nature and low cost.[22] However, compared to the precious metals-based catalysts, Co$_3$O$_4$ still exhibits a relatively lower catalytic activity, which has unfortunately limited its large-scale applications.[14] The easy accumulation and low conductivity of pure Co$_3$O$_4$ decrease the active sites and hinder the transport of electrons or protons.[23-25] Fortunately, recent studies found that catalysts based absolutely on combined oxides can bring about an increase in the real electrocatalytic activity, which may be attributed to the synergetic or heterojunction effect between the oxide components.[26] Some bi-functional materials have already been reported yet, such as NiFe LDH,[27] Co/MoO$_x$ (ref. 28) and Co, CoO$_x$@CN,[25] with the overall water splitting activities of 1.7 V, 1.72 V and 1.60 V, respectively, to reach the current density of 10 mA cm^{-2}. Therefore, the synergetic effect between combined oxide components needs to be further explored aiming to develop composite oxide catalysts with higher activity and stability.

Metal–organic frameworks (MOFs), with its high surface area, hybrid features and tunable porosity, multi-functionality and good catalytic selectivity, have drawn much more attention and are very attractive precursors for constructing nanostructured metal (oxide)/carbon and their nanocomposites by taking advantage of the unique thermal behavior and chemical reactivity.[29-31] As a result, MOFs should be a class of ideal

[a]Hefei National Laboratory for Physical Science at Microscale, Department of Materials Science & Engineering, Collaborative Innovation Center of Suzhou Nano Science and Technology, University of Science and Technology of China, Hefei 230026, China. E-mail: cqw@ustc.edu.cn

[b]High Magnetic Field Laboratory, Hefei Institutes of Physical Science, Chinese Academy of Sciences, Hefei 230031, China

precursors to prepare metals, alloys, and metallic oxides, thus emerging as a new platform in various fields.[30–32]

Herein, we report a simple and facile strategy to synthesize a bi-functional MOF-derived RuO_2/Co_3O_4 heterojunction electrocatalyst that is active for both HER and OER in alkaline solutions. A Co-based metal–organic framework (Co-BTC) was chosen as precursor for synthesizing designed RuO_2/Co_3O_4 by a two-step transformation from MOFs. The high catalytic activity of RuO_2/Co_3O_4 is originated from the fast charge-transfer kinetics resulting from the interface between Co_3O_4 and RuO_2.

Experimental

Material preparation

All reagents used were of analytical grade and used as received. Cobalt(II) acetate tetrahydrate ($C_4H_6CoO_4 \cdot 4H_2O$), 1,3,5-benzenetricarboxylic acid (H_3BTC), polyvinylpyrrolidone (($C_6H_9NO)_n$, PVP), ethanol (CH_3CH_2OH) was purchased from Sinopharm Chemical Reagent Co. Ltd (Shanghai, China), Ruthenium(III) chloride trihydrate ($RuCl_3 \cdot H_2O$), Nafion@perfluorinated resin solution. Deionized water was used throughout this work.

Syntheses of Co-BTC and Co_3O_4

Co-BTC used as MOF precursors was prepared according to the method described in the related literatures with some modifications.[33,34] For synthesis of Co-BTC, 0.2 g $C_4H_6CoO_4 \cdot 4H_2O$ and 1.2 g PVP was dissolved into the mixed solution of ethanol (20 mL) and deionized water (20 mL), formed solution A, which was put on the magnetic stirrer with a low speed. 0.36 g H_3BTC was dissolved into the mixed solution of ethanol (20 mL) and deionized water (20 mL), formed solution B. Then solution B was poured into solution A with a constant speed by using an injector (10 mL). The mixed solution was kept stirring until the precipitation formed. Finally, the product was centrifuged after 24 hours' standing and washed four times by ethanol before drying at 60 °C in vacuum. The powder of Co-BTC was placed in a tube furnace and heated to the desired temperature (500, 550, 600, and 650 °C) for 1 h under air atmosphere with a heating rate of 10 °C min^{-1} to obtain Co_3O_4-x, where "x" represents the carbonization temperature.

Syntheses of RuO_2/Co_3O_4

For synthesis of RuO_2/Co_3O_4, the powder of Co-BTC (50 mg) was dispersed in the solution of ethanol (20 mL) and deionized water (20 mL), stirring for 30 minutes. Then the well-prepared $RuCl_3$ (10 mg mL^{-1}, dissolved in deionized water) was added to the Co-BTC dispersion with different mole ratios (where Co : Ru equal to 10 : 1, 8 : 1, 6 : 1, and 4 : 1, respectively). The whole system was kept stirring for 24 h, then centrifugal separation and washed four times by ethanol before drying at 60 °C in vacuum. Finally, the product was placed in a tube furnace and heated to desired temperature (500, 550, 600, and 650 °C) for 1 h under air atmosphere with a heating rate of 10 °C min^{-1}.

Materials characterization

The powder XRD patterns of the samples were recorded with an X-ray diffractometer (Japan Rigaku D/MAX-γA) using Cu-Kα radiation ($\lambda = 1.54178$ Å) with a 2θ range of 20–80°. SEM images were taken by a JEOL JSM-6700M scanning electron microscope. TEM images were obtained with HitachiH-800 transmission electron microscope using an accelerating voltage of 200 kV, and HRTEM (JEOL-2011) was operated at 200 kV. TGA of Co-BTC and RuO_2/Co_3O_4 was carried out using a Shimadzu-50 thermoanalyser under flowing nitrogen at a heating rate of 10 °C min^{-1}. XPS was measured on an ESCALAB 250 X-ray photoelectron spectrometer using Al Kα radiation. The binding energies were calibrated based on the graphite C 1s peak at 284.8 eV. The XPS peakfit program with a Gaussian–Lorentzian mixed function and Shirley background subtraction was used to analyses the spectra. Inductively coupled plasma (ICP) data was obtained by using an Optima 7300 DV instrument. The specific surface and pore diameters were obtained from the results of N_2 physisorption at 77 K (Micromeritics ASAP 2020) by using BET (Brunauer–Emmet–Teller) and BJH (Barrett–Joyner–Halenda) methods, respectively. Raman spectra were obtained using a LabRAM HR Raman spectrometer.

Electrochemical measurement

All of the electrochemical measurements were performed in a three-electrode system on an electrochemical workstation (CHI 660D) in 1 M KOH electrolyte. Typically, 4 mg of catalyst and 30 μL Nafion solution (Sigma Aldrich, 5 wt%) were dispersed in 1 mL ethanol solution by sonicating for 1 h to form a homogeneous ink. Then 5 μL of the dispersion (containing 20 μg of catalyst) was loaded onto a glassy carbon electrode with 3 mm diameter (loading 0.285 mg cm^{-2}). While a Ag/AgCl (in 3 M KCl solution) electrode and a platinum foil were served as the reference electrode and counter electrodes, respectively. All of the potentials were calibrated to a reversible hydrogen electrode (RHE). The working electrode was polished with Al_2O_3 powders with size ranging from 1 μm down to 0.05 μm. Linear sweep voltammetry with a scan rate of 2 mV s^{-1} was conducted between −0.4 V and 0.1 V (vs. RHE) into 1 M KOH electrolyte with a stable flow of N_2 gas maintained over the electrolyte during the HER experiment. Cyclic voltammetry (CV) was conducted in 1 M KOH solution in the potential region from −0.4 V and 0.1 V (vs. RHE) at a sweep rate of 100 mV s^{-1} for 10 000 times to investigate the cycling stability. The same method is also applicable for OER process except that the LSV and CV curve was conducted between 1.20 V and 1.72 V (vs. RHE) with a scan rate of 5 mV s^{-1}.

Results and discussion

Characterization of MOF-derived Co_3O_4

The synthesis process for the RuO_2/Co_3O_4 heterojunction was illustrated in Scheme 1. The SEM and TEM images of the MOF-derived Co-BTC particles, illustrated respectively in Fig. 1a and b, suggest that it is a well-shaped rectangular bar in the range 15–20 μm in length and about 500 nm in diameter with a relatively smooth surface.

Scheme 1 Synthetic route for RuO_2/Co_3O_4.

The products of Co_3O_4 were prepared by annealing the precursors Co-BTC under air atmosphere. The sample annealed at 650 °C is named as S-650. Similar products obtained with the same annealing strategy under different temperatures refer to compounds S-600, S-550, and S-500.

The typical XRD patterns of precursors are shown in Fig. 1c. The diffraction peaks of the precursors are consistent with the values of Co-BTC reported by previous research.[33,35] The XRD patterns of annealed products are shown in Fig. 1d. The strong and sharp reflection peaks and the smooth baseline of S-650 indicate that the sample is well crystallized. It can be seen that no other impurity is presented in the sample except for the Co_3O_4. Similar XRD patterns are also observed for compounds S-600, S-550, and S-500. The obvious diffraction peaks can be identified for the (220), (311), (222), (400), (422), (511), (440), and (531) planes of cubic Co_3O_4 with a space group of $Fd\bar{3}m$ (227), which is consistent with the standard pattern of the Co_3O_4 (JCPDS: 42-1467). Raman spectroscopy has also been performed to determine the structural features that the sample is not carbonized (Fig. 2c, S-600).

Characterization of RuO_2/Co_3O_4

We get the final products RuO_2/Co_3O_4 by simply mixing Co-BTC with different amounts of $RuCl_3$ and then annealing at 600 °C under air atmosphere. The sample prepared from nominal composition Ru : Co molar ratio of 1 : 4 is named as S-4. Similar structures have also been obtained with the same annealing strategy for reference compounds S-6, S-8, and S-10.

The corresponding XRD patterns of the Co–Ru complex precursors were shown in Fig. 2a. The characteristic peaks show little difference with pure Co-BTC (yellow), indicating that the structure of Co–Ru complex stay the same with MOF Co-BTC. The XRD patterns of annealed products are shown in Fig. 2b. We can see that all samples are well crystallized. XRD patterns of the four samples are similar with each other and the peaks of Co_3O_4 and RuO_2 are both detected in four samples. The diffraction peaks appearing at $2\theta = 31.27°, 36.85°, 38.54°, 44.81°, 55.65°, 59.35°, 65.23°,$ and $68.63°$ are respectively correspond to the same crystalline planes with standard pattern of Co_3O_4 (JCPDS: 42-1467). While the diffraction peaks occurring at $2\theta = 28.02°, 35.07°, 40.04°,$ and $54.27°$ are indexed well to the (110), (101), (200), and (211) crystalline planes of RuO_2 (JCPDS: 43-1027). Raman spectroscopy of S-6 is shown in Fig. 2c. As one can see, the peaks of S-6 have an obvious shift to the left compared with the pure Co_3O_4 (black line), suggesting that there may be some interaction between Co_3O_4 and RuO_2.

The valence state of the components on the catalyst surface is identified by X-ray photoelectron spectroscopy (XPS) to confirm the formation of Co_3O_4 and RuO_2 (Fig. 2d–f). As shown in Fig. 2d, the presence of the Co $2p_{3/2}$ peak at 779.89 eV and the Co $2p_{1/2}$ peak at 795 eV indicates the formation of the Co_3O_4 phase.[22,36–39] The XPS spectrum of RuO_2 in the Ru 3p region (Fig. 2e) shows the peaks for Ru $3p_{3/2}$ at 462.8 eV and Ru $3p_{1/2}$ at 486.1 eV, which are attributed to the photoemission from RuO_2
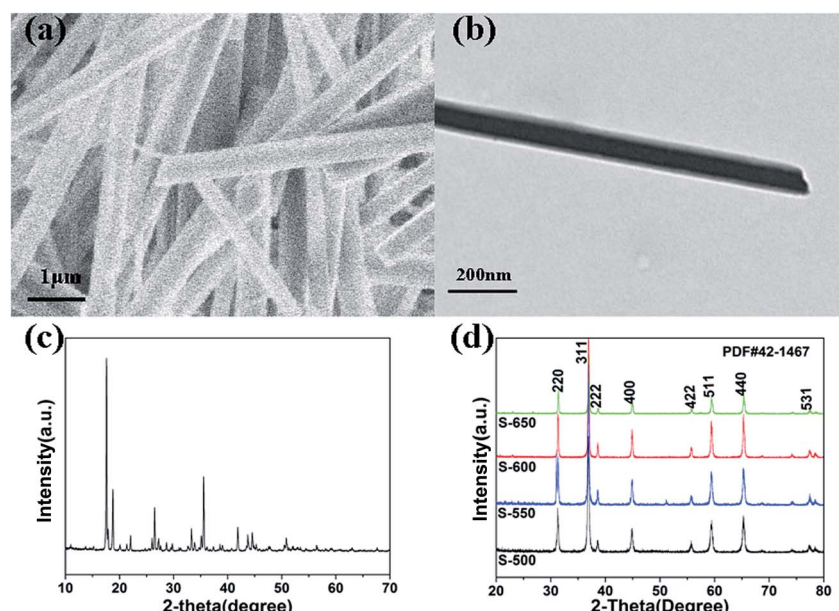

Fig. 1 (a) SEM image of Co-BTC. (b) TEM image of Co-BTC. (c) XRD patterns of Co-BTC. (d) XRD patterns of the Co_3O_4 samples (S-650, S-600, S-550, S-500).
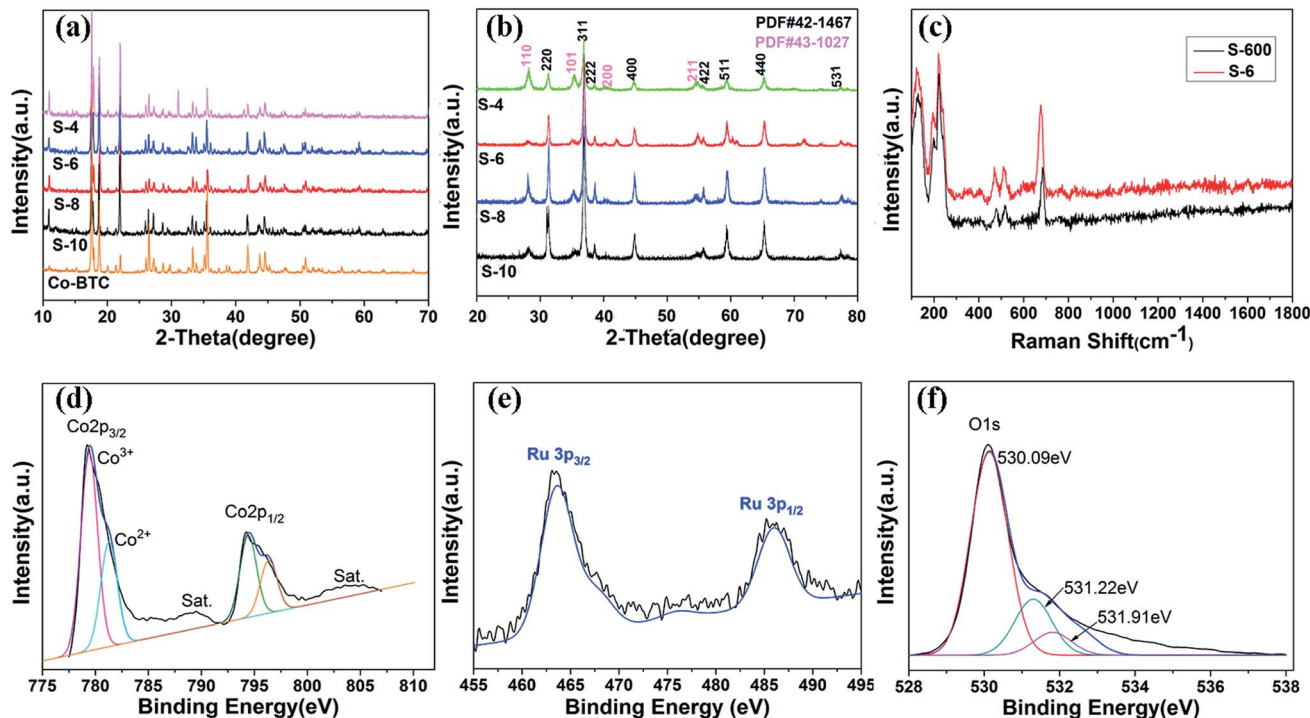
Fig. 2   XRD patterns of the Co−Ru complex precursors (a) and the annealed samples (b) (S-4, S-6, S-8, S-10). Raman spectra of Co_3O_4 (S-600) and Co_3O_4/RuO_2 (S-6) (c); XPS spectra of S-6 (d−f) (Co-in-S-6 (d); Ru-in-S-6 (e); O-in-S-6 (f)).

(Ru^{4+}).[40] The O 1s peak shown in Fig. 2f corresponds to metal–oxygen bonds as we expected.[39] The peaks centered at 530.09 eV and 531.22 eV correspond to oxygen species in the Co_3O_4 phase, while 531.91 eV correspond to oxygen species in the RuO_2 phase.[41,42] The shift of binding energy for Co and Ru reveals that there is an interaction between the metal atoms and O atoms, which is consistent with our previous results.

The SEM and TEM images of the Co–Ru complex precursor and annealed products S-6 were shown in Fig. 3a–c. It is clear to see that both the precursor and the air-annealed samples show the rectangular bar structure of Co–MOF, with some deposits on the surface. From Fig. 3c, we can get detailed structure information of S-6, which indicates that the annealed sample owns a long bar structure with metal oxides distributed along it. The dark part refers to RuO_2 and the light part represents Co_3O_4. It can also be proved by further HRTEM analysis shown in Fig. 4a, which confirms that the nanocomposites are composed of noble metal oxide RuO_2 and transition metal oxide Co_3O_4. The lattice fringes can be clearly observed in HRTEM image, in

which the 2.43 Å is in agreement with the (311) plane of Co_3O_4, while the 3.18 Å belongs to the (110) plane of RuO_2, respectively. It is worth noting that Fig. 4a also reveals the apparent crystal boundary between the Co_3O_4 nano-crystal and the RuO_2 nano-crystal. The boundaries demonstrate the generation of RuO_2/Co_3O_4 heterojunctions. In the heterojunctions, RuO_2 and Co_3O_4 particles closely connect to each other on a nano-level. The images of both EDS line profiles along the yellow line recorded on a random single small particle (Fig. 4b) and the corresponding elemental mapping (Fig. 4c–e) reveal that the Co, Ru and O are closely connected and well-distributed to each other at the nano-level. Element contents of S-6 were determined by ICP. The result indicates that atom ratio of Co and Ru is exactly to be 29.3 : 0.79. This result is somewhat different from the EDS line scan result, which shows that Co : Ru = 39.09 : 2.96. RuO_2 tends to be extremely stable in both acidic and alkaline solution although tremendous efforts have been made to dissolve it, which results in the large difference between them.
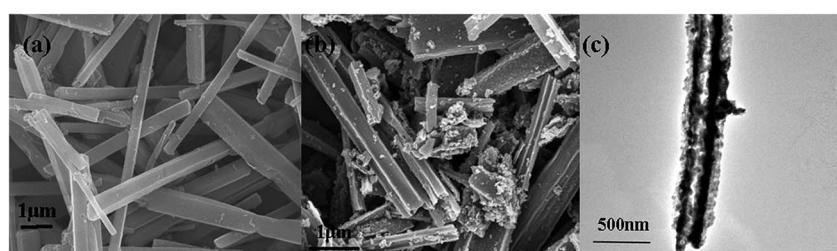

Fig. 3   SEM images of Co−Ru complex precursor (a) and S-6 (b). TEM image of S-6 (c).
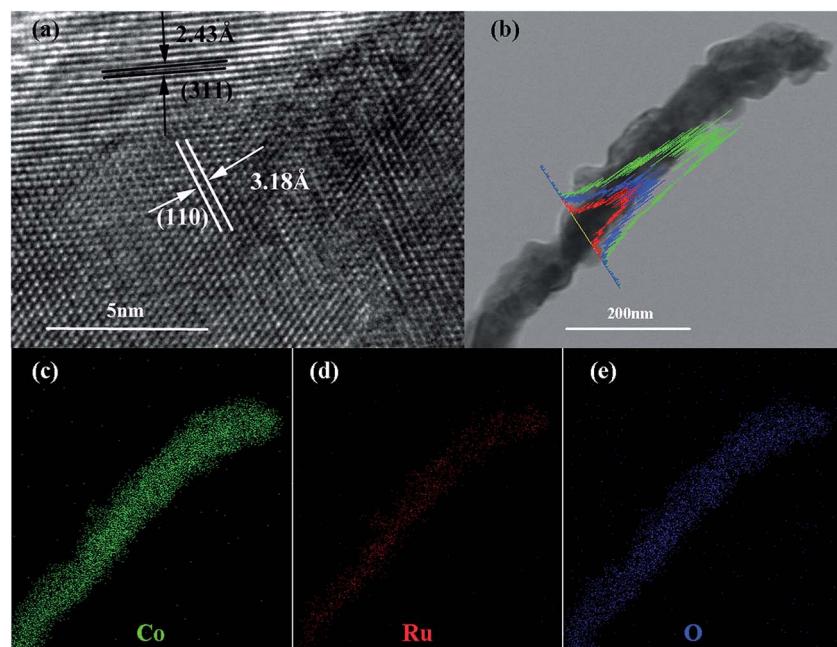
Fig. 4 HRTEM of S-6 (a); TEM image of the RuO_2/Co_3O_4 nanocrystalline–scan EDS analysis across the nanocrystal (b); elemental mappings of Co (c); Ru (d); O (e).

Electrochemical properties of Co_3O_4 and Co_3O_4/RuO_2

The electrochemical catalytic activity of the samples for OER is recorded using a typical three-electrode electrochemical cell in N_2-saturated 1 M KOH electrolyte. The OER performance is evaluated by observing the overpotential at 10 mA cm^{-2} *versus* a reversible hydrogen electrode (RHE). The polarization curves of Co_3O_4 annealed at different temperatures are shown in Fig. 5a. The trend in the overpotential can be concluded as S-500

(482 mV) < S-550 (435 mV) < S-600 (423 mV) > S-650 (457 mV), suggesting that the S-600 catalyst has the highest OER activity among four catalysts with an overpotential of 423 mV without *iR*-correction. Fig. 5b displays the LSV curves of the final samples synthesized in different molar ratios and annealed at 600 °C, which throw light on the main overpotential changes against each other. That is S-10 (377 mV) < S-8 (353 mV) < S-6 (305 mV) > S-4 (338 mV). With the amount of RuO_2 increase, the overpotential of the samples decreases until the molar ratio
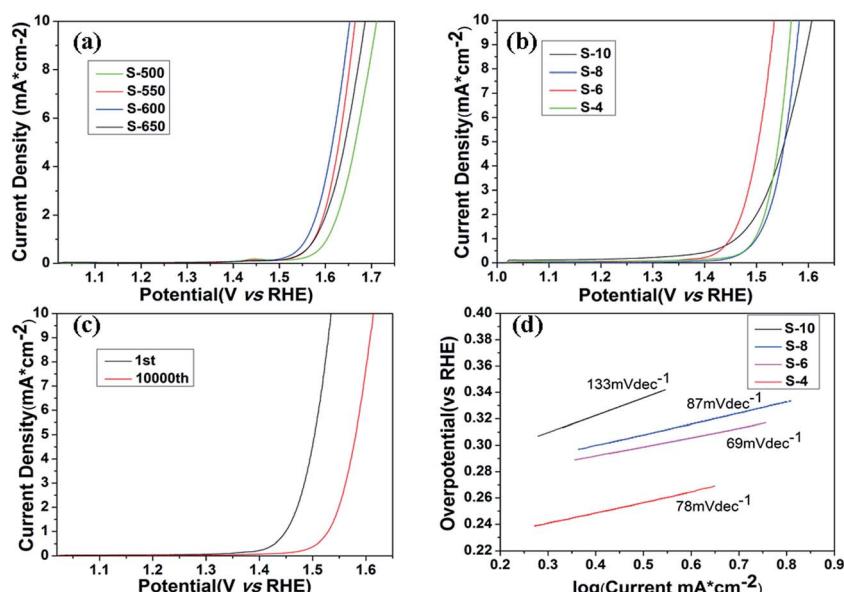
Fig. 5 OER polarization curves of Co_3O_4 samples annealed at different temperature (a); and RuO_2/Co_3O_4 complex with different molar ratios (b) in 1 M KOH; polarization curves of S-6 after the 1st and 10 000th cycles (c); Tafel plots of S-4, S-6, S-8, and S-10 (d).

reaches an extreme point (nominal starting molar Co : Ru = 6 : 1). Further addition of RuO_2 only received a counterproductive effect. We can also come to a conclusion as follows. Despite the small content of RuO_2 (Co : Ru refers to 39.09 : 2.96), the overpotential of combined mental oxides still presents obvious ascension than the best performance of Co_3O_4 samples from the above data, which may be attributed to the synergetic effect between the oxide components. It is also much better than commercial RuO_2 catalyst (377 mV) according to the previous research reported by our group.[15] Tafel slope (Fig. 5d) of the S-6 sample is 69 mV dec^{-1}, which is slightly better than the value of S-4 (78 mV dec^{-1}), S-8 (87 mV dec^{-1}) and S-10 (133 mV dec^{-1}), indicating that S-6 drives the OER process at a lower overpotential than the other four samples.

In addition, durability is another important parameter in the exploration of electrocatalyst. A cycling test was applied with polarization curves at an accelerated scanning rate. The polarization curve of S-6 after 10 000 cycles is displayed in Fig. 5c. The overpotential of S-6 increased by 79 mV to reach a result of 384 mV, which is obviously superior to the durability of commercial RuO_2.[15] Therefore, the S-6 sample has a higher activity and durability than commercial RuO_2 catalysts.

HER activities are also examined by observing the overpotential at 10 mA cm^{-2} in N_2-saturated 1 M KOH electrolyte under the same condition. The LSV curves of Co_3O_4 annealed at different temperatures are displayed in Fig. 6a. Apparently, the overpotential goes down with the anneal temperature increases. The overpotential of S-500, S-550, S-600 and S-650 are 387 mV,

375 mV, 351 mV and 379 mV, respectively, indicating that the best performance of the Co_3O_4 samples occurs at a anneal temperature of 600 °C. Further studies are done based on this result. Polarization curves of RuO_2/Co_3O_4 metal oxide products were shown in Fig. 6b. To achieve a current density of 10 mA cm^{-2}, the S-10, S-8, S-6 and S-4 require overpotential of 189 mV, 155 mV, 89 mV and 140 mV, respectively, which is much lower than the best performance of Co_3O_4 (351 mV) displayed above, revealing that our synthesized nanocomposites are effective catalysts for HER in alkaline solution.

The stability of S-6 is also tested by a cycling test of 10 000 (Fig. 6c). There is a slight decrease emerging after 10 000 cycles in alkaline environment, displaying an excellent durability. Besides, I–t curve is also taken for further validation. The stable current density over 10 h of continuous operation at an applied overpotential of 89 mV in alkaline media is presented in Fig. 6d. It remains almost steady for 40 000 s.

To investigate the kinetics of the HER process promoted by as-prepared catalysts, Tafel plots analyses are carried out (Fig. 6e). The present study shows that S-6 gives a Tafel slope of 91 mV dec^{-1}, lower than that of S-4 (103 mV dec^{-1}), S-8 (121 mV dec^{-1}) and S-10 (122 mV dec^{-1}), implying its favorable HER catalytic kinetics in alkaline solution. As the rate-determining step (RDS) is reflected by Tafel slope of a catalyst, the variation of the Tafel slope can be explained by the change of RDS in the HER process. Based on the data of the four Tafel slope, Volmer–Heyrovsky mechanism can be determined.
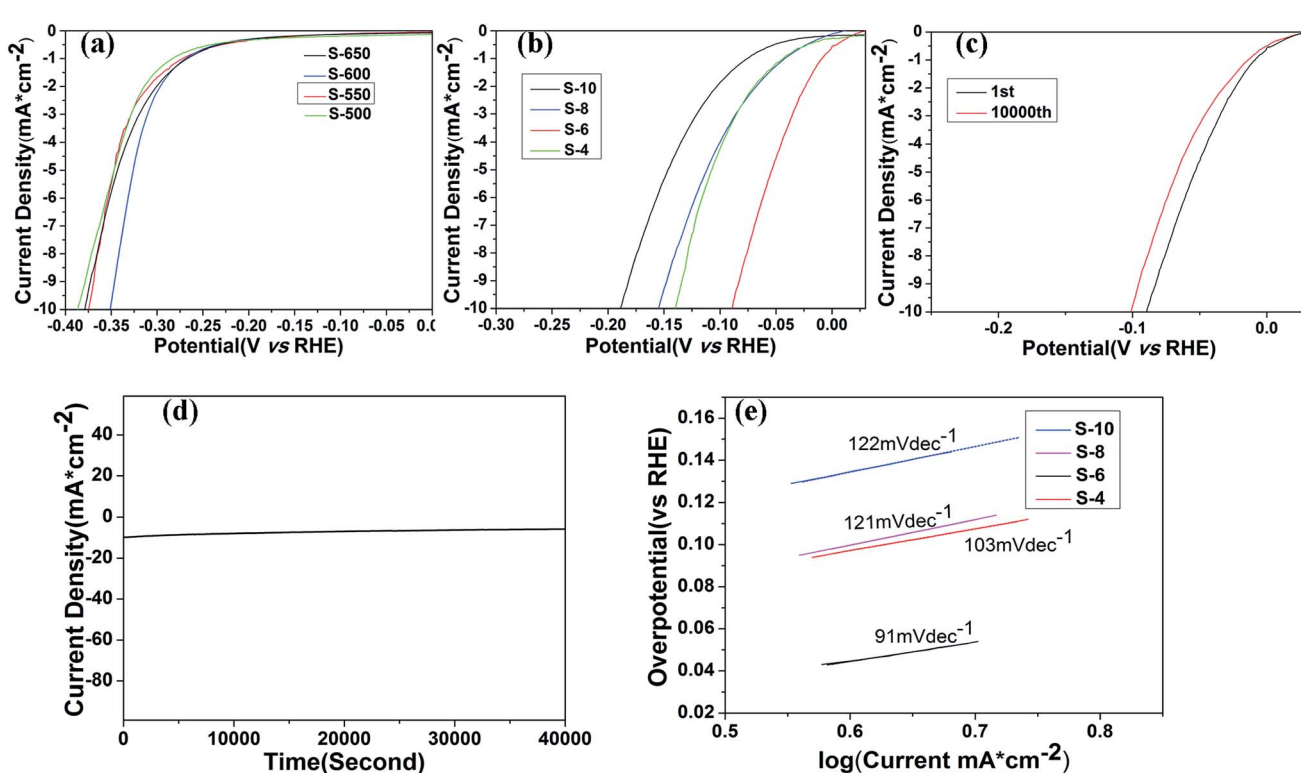

Fig. 6 HER polarization curves of Co_3O_4 samples annealed at different temperature (a); and RuO_2/Co_3O_4 with different molar ratios (b) in 1 M KOH; polarization curves of S-6 after the 1st and 10 000th cycles (c); chronoamperometry measurements (I vs. t) recorded on S-6 at a constant applied potential of 89 mV vs. RHE (d) Tafel plots of S-4, S-6, S-8, and S-10 (e).
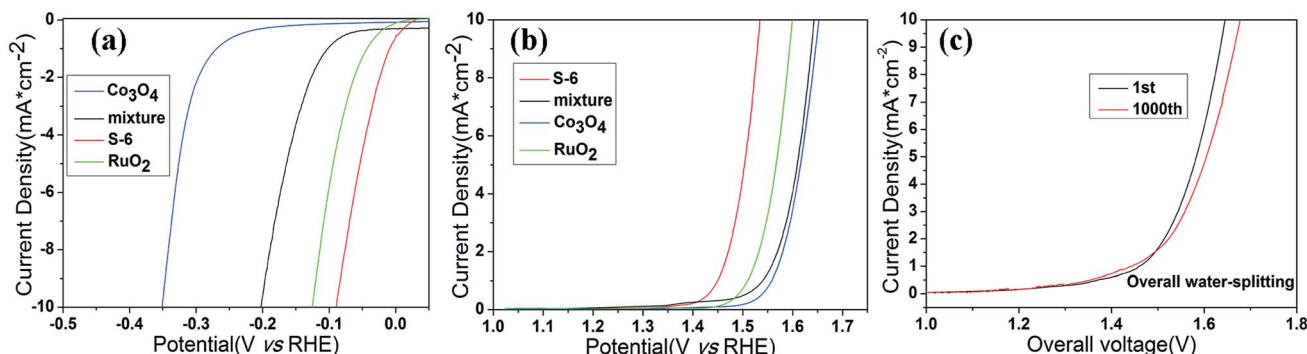
Fig. 7 HER (a) and OER (b) polarization curves of RuO_2/Co_3O_4, Co_3O_4 and the mixture of Co_3O_4 and RuO_2. (c) Overall water-splitting characteristics of $RuO_2/Co_3O_4 \| RuO_2/Co_3O_4$ in two-electrode configurations in 1 M KOH. All the data are without iR-compensation.

With the aforementioned excellent HER and OER catalytic performance of RuO_2/Co_3O_4 in hand, we are confident that it can act as an electrocatalyst for both HER and OER in alkaline solution. As is concluded above, this material shows a low OER and HER overpotential of only 305 mV and 89 mV at 10 mA cm^{-2} of current density in alkaline solution, respectively. Such a superior electrocatalytic performance may be attributed to its unique properties. Transition metal oxide with metal–organic frameworks are known to be very active HER electrocatalysts, while RuO_2 owns a perfect activity towards OER process. Once they combined together, they will contribute to the overall water splitting. In order to confirm the synergetic effect of the nano-interfaces in RuO_2/Co_3O_4, a group of controlled trials are taken by simply mix the two compounds (Co_3O_4 and RuO_2) together and test the LSV values of the mixture. The HER and OER polarization curves are displayed in Fig. 7a and b. The mixture reaches a current density of 10 mA cm^{-2} at overpotentials of 413 mV for OER and 203 mV for HER, respectively. We can clearly find that the performance of RuO_2/Co_3O_4 proves to be much better than the mixture. RuO_2 may be responsible for the

electrochemistry performance, however, the interface of Co_3O_4 and RuO_2 enhance its electrochemical activity. Further electrochemically active surface area (ECSA) experiments have shown that the high performance of the product could be caused by the increased active sites at the interface of RuO_2/Co_3O_4 heterojunction (Fig. S1†).

The bifunctional RuO_2/Co_3O_4 were further investigated as the same electrocatalyst on both electrodes with a two-electrode configuration to test the activity for overall water splitting in 1 M KOH (Fig. 7). The liner sweep voltammetry of the $RuO_2/Co_3O_4 \| RuO_2/Co_3O_4$ system shows that the current density of 10 mA cm^{-2} is achieved at a voltage of 1.645 V. This value changes to 1.678 V after 1000 cycles, showing a decrease in activity. Also, we have compared the electrocatalytic performances of RuO_2/Co_3O_4 with a series of related catalysts listed in Table 1. It is shown that no Co_3O_4-based material serves as bi-functional catalysts in water splitting progress at present stage. Moreover, Co_3O_4-based catalysts towards HER are not reported as much as that of OER. Even though the reported Co/Co_3O_4 owns a similar overpotential of 90 mV towards HER in 1 M KOH

Table 1 Comparison of electrocatalytic performances of related materials at 10 mA cm^{-2} of current density in alkaline solution

Catalyst	Catalyst loading (mg cm^{-2})	Electrolyte	HER overpotential (mV)	OER overpotential (mV)	OWS potential (V)	Reference
$Cu_xCo_{3-x}O_4$	—	1 M KOH	—	410		43
$Ni_xCo_{3-x}O_4$	0.7	1 M KOH	—	337	—	44
$NiCo/NiCoO_x$	0.7	1 M KOH	155	—	—	44
$Zn_xCo_{3-x}O_4$	1.0	1 M KOH	—	320	—	45
Co_3O_4 shell/Au core NPs	0.2	0.1 M KOH	—	390	—	46
Plasma-engraved Co_3O_4	—	0.1 M KOH	—	300	—	47
Co/Co_3O_4	0.85	1 M KOH	90	—	—	48
Co_3O_4/N-graphene + Ni foam	0.17	1 M KOH	—	310	—	49
Co_3O_4 NPs/Ni foam	0.2	1 M KOH	—	360	—	50
meso-Co_3O_4	0.1	0.1 M KOH	—	411	—	51
Co_xO_y/NC	0.21	0.1 M KOH	—	430	—	52
Co_3O_4–carbon	—	0.1 M KOH	—	290	—	53
Co, CoO_x@CN	0.42	1 M KOH	232	260	1.60	25
Co/MoO_x	0.7	1 M KOH	40(onset)	230(onset)	1.72	28
Ni–RuO_2	4.2	1 M NaOH	115(100)	—	—	54
Mn_xO_y/RuO_2	—	1 M KOH	—	312		55
RuO_2/Co_3O_4	0.285	1 M KOH	89	305	1.645	This work

compared with our RuO_2/Co_3O_4, its OER activity in alkaline solution is absent. Therefore, it is concluded that RuO_2/Co_3O_4 has a competitive performance towards both HER and OER in alkaline solution. The combination of Co_3O_4 and RuO_2 provides an interface that owns highly active catalytic sites in electrochemistry, which may be attributed to the structure of heterojunction.[31] Previous density-functional theory (DFT) calculations revealed that interface show significantly increased DOS at the band edge with respect to combined oxides, resulting in improvement of the catalytic performance.[15,31,56] This is the main reason why our material performs much better than many other Co_3O_4-based catalysts.

Conclusions

In summary, we adopt a MOF-annealing strategy to synthesize a combined metal oxide RuO_2/Co_3O_4 as an efficient bifunctional electrocatalyst towards OER and HER in alkaline solution. The catalyst exhibited excellent activity with low overpotential, small Tafel slope, as well as an outstanding electrochemical durability in HER evaluation even after the 10 000th cycling. The stability in OER also performs even better than commercial RuO_2. This work shows that a heterojunction composed by transition metal oxides with small amounts of noble metal oxides can provide more active sites for OER and HER electrocatalysts with high performance.

Acknowledgements

References

1 L. Yu, B. Y. Xia, X. Wang and X. W. Lou, *Adv. Mater.*, 2016, **28**, 92–97.

2 M. K. Debe, *Nature*, 2012, **486**, 43–51.

3 C. C. L. McCrory, S. Jung, I. M. Ferrer, S. M. Chatman, J. C. Peters and T. F. Jaramillo, *J. Am. Chem. Soc.*, 2015, **137**, 4347–4357.

4 F. Song and X. Hu, *Nat. Commun.*, 2014, **5**, 4477.

5 B. You, N. Jiang, M. Sheng, S. Gul, J. Yano and Y. Sun, *Chem. Mater.*, 2015, **27**, 7636–7642.

6 M. G. Walter, E. L. Warren, J. R. McKone, S. W. Boettcher, Q. Mi, E. A. Santori and N. S. Lewis, *Chem. Rev.*, 2010, **110**, 6446–6473.

7 A. J. Esswein, M. J. McMurdo, P. N. Ross, A. T. Bell and T. D. Tilley, *J. Phys. Chem. C*, 2009, **113**, 15068–15072.

8 B. Seo, Y. J. Sa, J. Woo, K. Kwon, J. Park, T. J. Shin, H. Y. Jeong and S. H. Joo, *ACS Catal.*, 2016, **6**, 4347–4355.

9 A. Indra, P. W. Menezes, N. R. Sahraie, A. Bergmann, C. Das, M. Tallarida, D. Schmeisser, P. Strasser and M. Driess, *J. Am. Chem. Soc.*, 2014, **136**, 17530–17536.

10 T. Maiyalagan, K. A. Jarvis, S. Therese, P. J. Ferreira and A. Manthiram, *Nat. Commun.*, 2014, **5**, 3949.

11 J. Chang, Y. Xiao, M. Xiao, J. Ge, C. Liu and W. Xing, *ACS Catal.*, 2015, **5**, 6874–6878.

12 J. Li, Y. Wang, T. Zhou, H. Zhang, X. Sun, J. Tang, L. Zhang, A. M. Al-Enizi, Z. Yang and G. Zheng, *J. Am. Chem. Soc.*, 2015, **137**, 14305–14312.

13 J. B. Gerken, J. G. McAlpin, J. Y. C. Chen, M. L. Rigsby, W. H. Casey, R. D. Britt and S. S. Stahl, *J. Am. Chem. Soc.*, 2011, **133**, 14431–14442.

14 Y. Sun, S. Gao, F. Lei, J. Liu, L. Liang and Y. Xie, *Chem. Sci.*, 2014, **5**, 3976.

15 J. Su, G. Xia, R. Li, Y. Yang, J. Chen, R. Shi, P. Jiang and Q. Chen, *J. Mater. Chem. A*, 2016, **4**, 9204–9212.

16 J. Deng, P. Ren, D. Deng and X. Bao, *Angew. Chem.*, 2015, **54**, 2100–2104.

17 J. Deng, P. Ren, D. Deng, L. Yu, F. Yang and X. Bao, *Energy Environ. Sci.*, 2014, **7**, 1919.

18 Y. Yang, Z. Lun, G. Xia, F. Zheng, M. He and Q. Chen, *Energy Environ. Sci.*, 2015, **8**, 3563–3571.

19 M. Tavakkoli, T. Kallio, O. Reynaud, A. G. Nasibulin, C. Johans, J. Sainio, H. Jiang, E. I. Kauppinen and K. Laasonen, *Angew. Chem.*, 2015, **54**, 4535–4538.

20 Z. Lu, H. Wang, D. Kong, K. Yan, P.-C. Hsu, G. Zheng, H. Yao, Z. Liang, X. Sun and Y. Cui, *Nat. Commun.*, 2014, **5**, 4345.

21 J. Rosen, G. S. Hutchings and F. Jiao, *J. Am. Chem. Soc.*, 2013, **135**, 4516–4521.

22 C. Yuan, L. Yang, L. Hou, L. Shen, F. Zhang, D. Li. and X. Zhang, *J. Mater. Chem.*, 2011, **45**, 18183–18185.

23 Y. Fan, H. Shao, J. Wang, L. Liu, J. Zhang and C. Cao, *Chem. Commun.*, 2011, **47**, 3469–3471.

24 Y. Xu, R. Yi, B. Yuan, X. Wu, M. Dunwell, Q. Lin, L. Fei, S. Deng, P. Andersen, D. Wang and H. Luo, *J. Phys. Chem. Lett.*, 2012, **3**, 309–314.

25 H. Jin, J. Wang, D. Su, Z. Wei, Z. Pang and Y. Wang, *J. Am. Chem. Soc.*, 2015, **137**, 2688–2694.

26 L. M. Da Silva, J. F. C. Boodts and L. A. De Faria, *Electrochim. Acta*, 2001, **46**, 1369–1375.

27 J. Luo, J.-H. Im, M. T. Mayer, M. Schreier, M. K. Nazeeruddin, N.-G. Park, S. D. Tilley, H. J. Fan and M. Grätzel, *Science*, 2014, **345**, 1593–1596.

28 X. Yan, L. Tian, S. Atkins, Y. Liu, J. Murowchick and X. Chen, *ACS Sustainable Chem. Eng.*, 2016, **4**, 3743–3749.

29 H. Hu, L. Han, M. Yu, Z. Wang and X. W. Lou, *Energy Environ. Sci.*, 2016, **9**, 107–111.

30 C. Wang, D. Liu and W. Lin, *J. Am. Chem. Soc.*, 2013, **135**, 13222–13234.

31 R. Zhang, L. Hu, S. Bao, R. Li, L. Gao, R. Li and Q. Chen, *J. Mater. Chem. A*, 2016, **4**, 8412–8420.

32 Y. Z. Chen, C. Wang, Z. Y. Wu, Y. Xiong, Q. Xu, S. H. Yu and H. L. Jiang, *Adv. Mater.*, 2015, **27**, 5010–5016.

33 N. Yang, H. Song, X. Wan, X. Fan, Y. Su and Y. Lv, *Analyst*, 2015, **140**, 2656–2663.

34 F. Zheng, G. Xia, Y. Yang and Q. Chen, *Nanoscale*, 2015, **7**, 9637–9645.

35 O. M. Yaghi, H. L. Li and T. L. Groy, *J. Am. Chem. Soc.*, 1996, **118**, 9096–9101.

36 J. Wu, Y. Xue, X. Yan, W. S. Yan, Q. M. Cheng and Y. Xie, *Nano Res.*, 2012, **5**, 521–530.

37 H. Tuysuz, Y. Liu, C. Weidenthaler and F. Schuth, *J. Am. Chem. Soc.*, 2008, **130**, 14108–14110.

38 D. Oh, J. Qi, B. Han, G. Zhang, T. J. Carney, J. Ohmura, Y. Zhang, Y. Shao-Horn and A. M. Belcher, *Nano Lett.*, 2014, **14**, 4837–4845.

39 L. Huang, Y. Mao, G. Wang, X. Xia, J. Xie, S. Zhang, G. Du, G. Cao and X. Zhao, *New J. Chem.*, 2016, **40**, 6812–6818.

40 M. Gopiraman, R. Karvembu and I. S. Kim, *ACS Catal.*, 2014, **4**, 2118–2129.

41 S. Xiong, C. Yuan, X. Zhang, B. Xi and Y. Qian, *Chem.–Eur. J.*, 2009, **15**, 5320–5326.

42 D. Susanti, D. S. Tsai, Y. S. Huang, A. Korotcov and W. H. Chung, *J. Phys. Chem. C*, 2007, **111**, 9530–9537.

43 P. Bothra and S. K. Pati, *ACS Energy Lett.*, 2016, 858–862.

44 X. Yan, K. Li, L. Lyu, F. Song, J. He, D. Niu, L. Liu, X. Hu and X. Chen, *ACS Appl. Mater. Interfaces*, 2016, **8**, 3208–3214.

45 X. Liu, Z. Chang, L. Luo, T. Xu, X. Lei, J. Liu and X. Sun, *Chem. Mater.*, 2014, **26**, 1889–1895.

46 Z. Zhuang, W. Sheng and Y. Yan, *Adv. Mater.*, 2014, **26**, 3950–3955.

47 L. Xu, Q. Jiang, Z. Xiao, X. Li, J. Huo, S. Wang and L. Dai, *Angew. Chem.*, 2016, **55**, 5277–5281.

48 X. Yan, L. Tian, M. He and X. Chen, *Nano Lett.*, 2015, **15**, 6015–6021.

49 Y. Liang, Y. Li, H. Wang, J. Zhou, J. Wang, T. Regier and H. Dai, *Nat. Mater.*, 2011, **10**, 780–786.

50 A. Mendoza-Garcia, D. Su and S. Sun, *Nanoscale*, 2016, **8**, 3244–3247.

51 Y. J. Sa, K. Kwon, J. Y. Cheon, F. Kleitz and S. H. Joo, *J. Mater. Chem. A*, 2013, **1**, 9992–10001.

52 J. Masa, W. Xia, I. Sinev, A. Zhao, Z. Sun, S. Grutzke, P. Weide, M. Muhler and W. Schuhmann, *Angew. Chem.*, 2014, **53**, 8508–8512.

53 T. Y. Ma, S. Dai, M. Jaroniec and S. Z. Qiao, *J. Am. Chem. Soc.*, 2014, **136**, 13925–13931.

54 N. Spataru, J. G. LeHelloco and R. Durand, *J. Appl. Electrochem.*, 1996, **26**, 397–402.

55 A. J. Jeevagan, Y. Suzuki, T. Gunji, G. Saravanan, Y. Irii, T. Tsuda, T. Onobuchi, S. Kaneko, G. Kobayashi and F. Matsumoto, *ECS Trans.*, 2014, **58**, 9–18.

56 S. Bao, N. Yan, X. Shi, R. Li and Q. Chen, *Appl. Catal., A*, 2014, **487**, 189–194.